

# Multi-Layer Kesterite-Based Photocathodes for NH<sub>3</sub> Photosynthesis from N<sub>2</sub> Reduction Reaction

Juliana Ferreira de Brito,<sup>\*[a]</sup> Marina Medina,<sup>[a, b]</sup> Hugo Leandro Sousa Santos,<sup>[b]</sup> Mileny dos Santos Araujo,<sup>[b]</sup> Marcos Antônio Santana Andrade, Jr.,<sup>[b]</sup> and Lucia Helena Mascaro<sup>[b]</sup>

The necessity of new methods to substitute the Haber-Bosch process in the NH<sub>3</sub> synthesis, generating fewer greenhouse gases, and dispensing less energy, drove the investigation of the photoelectrocatalytic approach in the N<sub>2</sub> reduction reaction (N<sub>2</sub>RR). For that, this work presents the synthesis and characterization of the layered CZTSSe/CdS/TiO<sub>2</sub> photocathode decorated with Pt nanoparticles for application in NH<sub>3</sub> production using the photoelectrocatalysis technique. The CZTSSe/CdS/TiO<sub>2</sub>-Pt characterization showed a well-designed and stable photocatalyst synthesized layer by layer with an important contribution of the Pt nanoparticles for the catalyst performance, improving the photocurrent density and the charge transfer. The N<sub>2</sub>RR in a two-compartment photochemical cell

with 0.1 mol L<sup>-1</sup> Na<sub>2</sub>SO<sub>3</sub> and 0.05 mol L<sup>-1</sup> H<sub>2</sub>SO<sub>4</sub> in the cathodic and anodic chamber, respectively, using CZTSSe/CdS/TiO<sub>2</sub>-Pt and under 1 sun of light incidence and applied potential of -0.4 V<sub>Ag/AgCl</sub> reached 0.22 mmol L<sup>-1</sup> cm<sup>-2</sup> NH<sub>3</sub>, a value 28 folds higher than using the catalyst without Pt modification. The superiority of N<sub>2</sub>RR under the photoelectrocatalysis technique was demonstrated compared to photocatalytic and electrocatalytic techniques, together with the investigation of the supporting electrolyte influence in the cathodic compartment. Additionally, that is the first time a kesterite-based photocathode has been applied to NH<sub>3</sub> photosynthesis, showing excellent photoconversion capability.

## Introduction

Ammonia (NH<sub>3</sub>) is one of the main chemical products produced on a large scale, for use in fertilizer manufacture ensuring global food security.<sup>[1]</sup> It also can act as a hydrogen carrier and a green fuel due to its carbon-free nature.<sup>[2,3]</sup> The NH<sub>3</sub> production occurs mainly by the Haber-Bosch (HB) process, in which N<sub>2</sub> and H<sub>2</sub> react on the surface of iron- and ruthenium-based catalysts under high temperatures (450–500 °C) and pressures (200–300 atm) to surpass the elevated N<sub>2</sub> bond dissociation energy (945 kJ mol<sup>-1</sup>).<sup>[4]</sup> Beyond being energy-intensive, this process also contributes to greenhouse gas emissions, since the used H<sub>2</sub> is produced by methane steam reforming.<sup>[5]</sup> In this sense, the HB process does not align with the sustainable development goals dictated in the 2030 Agenda.

The environmentally sustainable N<sub>2</sub>-to-NH<sub>3</sub> conversion promoted by electrochemical nitrogen reduction reaction (E-NRR) is performed by renewable electricity, and aqueous as a proton source.<sup>[6]</sup> However, the poor solubility in aqueous solution, added to the inertness of the triple bond, remains the main challenge regarding the use of N<sub>2</sub> to promote NH<sub>3</sub> production.<sup>[7]</sup>

Beyond this, the multi-step reaction pathway involving six electrons leads to a sluggish mechanism kinetics.<sup>[8]</sup> Thus far, a set of catalysts including nonmetals,<sup>[9–11]</sup> noble metals,<sup>[12]</sup> and non-noble metals (Fe, Mo, Co, W, Ni) in the form of alloys,<sup>[13,14]</sup> chalcogenides,<sup>[15–17]</sup> carbides,<sup>[18]</sup> and oxides<sup>[19,20]</sup> have been developed for E-NRR. Nevertheless, the competition between E-NRR and the hydrogen evolution reaction (HER), remains a huge challenge.<sup>[21]</sup>

The requirement to improve the Faradaic efficiency (FE) of NH<sub>3</sub> production is a high catalytic current density with low H<sub>2</sub> production.<sup>[22]</sup> In this sense, with photoelectrochemical nitrogen reduction reaction (PEC-NRR) it is possible to mitigate the HER by positively shifting the applied potential, while the current density is maintained by generating additional photoelectrons.<sup>[23,24]</sup> Among the p-type semiconductors, kesterites Cu<sub>2</sub>ZnSn(S,Se)<sub>4</sub> (CZTSSe) have been widely used in PEC applications due to their excellent light absorption capability, mainly in the visible light range because of its optical band gap value of ~1.5 eV, and its earth-abundant raw elements.<sup>[25,26]</sup> The insertion of Se atoms in the CZTS optimizes the electric properties, leading to a decrease in surface defects.<sup>[27–29]</sup> It is common to accomplish extra layers in the photocathode assembly.<sup>[30–32]</sup> A CdS has been used to create a p-n junction, enabling an efficient charge separation rate, and a TiO<sub>2</sub> protecting layer, improving the photostability.<sup>[33,34]</sup> Also, the incorporation of a cocatalyst material is an interesting strategy to improve the catalytic cycle involving the N<sub>2</sub> adsorption, activation, and reduction processes.<sup>[35]</sup> By tailoring the cocatalyst deposition in the form of nanoparticles, it is possible to power the reaction kinetics, by improving the electron transfer in the catalyst/electrolyte interface, without interfering with the

[a] J. Ferreira de Brito, M. Medina  
Alternative Technologies of Detection, Toxicological Evaluation and Removal of Micropollutants and Radioactives (INCT-DATREM), Univ. Estadual Paulista – Institute of Chemistry – Araraquara, UNESP, Rua Francisco Degni, 55, Bairro Quitandinha, Araraquara, SP 14800-900, Brazil  
E-mail: juliana.f.brito@unesp.br

[b] M. Medina, H. L. Sousa Santos, M. dos Santos Araujo, M. A. Santana Andrade, Jr., L. Helena Mascaro  
Department of Chemistry, Federal University of São Carlos, Rod. Washington Luiz, Km 235, CEP 13565-905, São Carlos-SP, Brazil

photocathode light absorption capability.<sup>[36,37]</sup> The electrodeposition technique assisted by light incidence (photoelectrodeposition) for platinum (Pt) nanoparticles is a powerful approach to improve photocurrent density by increasing the number of available active sites on the semiconductor surface activated by the photons.<sup>[38]</sup>

In this work, we demonstrate for the first time the  $N_2$ -to- $NH_3$  conversion in a PEC system using a kesterite-based photocathode assembly, the CZTSSe/CdS/ $TiO_2$ -Pt semiconductor. The photoelectrodeposition of Pt nanoparticles as a cocatalyst effectively promoted surface reaction kinetics by improving the charge transfer in the photocathode/electrolyte interface. Additionally, the investigation of the supporting electrolyte's influence in the cathodic compartment was performed, showing the superiority of  $Na_2SO_3$  for  $NH_3$  production.

## Results and Discussion

### CZTSSe Electrode Characterization

In this study, CZTSSe was synthesized through the thermal selenization of CZTS thin films, easily deposited via spin coating on the FTO surface. The incorporation of selenium offers numerous benefits over CZTS, including a tunable band gap, enhanced optoelectronic properties (improved carrier mobility and lifetime), lowered bandgap energy, and improved photovoltaic performance, characterized by a higher open-circuit voltage.<sup>[39]</sup> Figure 1a displays the elemental distribution along the thickness of CZTSSe, as determined by glow-discharge optical emission spectrometry (GDOES). Importantly, the composition of CZTSSe remains relatively constant across the film's thickness. Additionally, the rise in Se and Mo intensities beyond 0.8  $\mu m$  depth is due to the formation of  $MoSe_2$  at the interface of CZTSSe/Mo. The selenization of CZTS to CZTSSe was proven by assessing the  $S/(S+Se)$  ratio using glow-discharge optical emission spectrometry (GDOES). As illustrated in Figure 1b, the surface composition of CZTSSe exhibited an elevated Se concentration, reflected in the  $S/(S+Se)$  ratio measuring below 5%. Moreover, there was a slight increment in S concentration with increasing film depth. Nevertheless, the overall selenization of CZTS can be considered successful. The films were fabricated under Cu-poor conditions, denoted by  $I/(II+IV)=0.75$ , and Zn-rich conditions, with  $II/IV=1.05$ . These specific ratios were chosen to avoid the formation of low band gap ternary phases, such as  $Cu_2SnS_3$ , which are prevalent in Cu-rich compositions and are potential contributors to a low open circuit voltage ( $V_{oc}$ ) in devices prepared under such conditions.<sup>[4]</sup> Hence, these ratios are optimal for achieving the highest efficiency in the CZTSSe device.<sup>[5-7]</sup> Elemental profiles shown in Figure 1c indicate the consistent maintenance of the Cu-poor condition across all compositions, with  $I/(II+IV)$  approximately 0.75. Although the  $II/IV$  elemental ratio varied between 1.06 and 1.19, all samples also exhibited Zn-rich characteristics.

The morphology of CZTSSe was assessed through surface SEM images. Figure 2a reveals a compact-grained surface for CZTSSe, featuring an average grain size of approximately 1  $\mu m$ ,

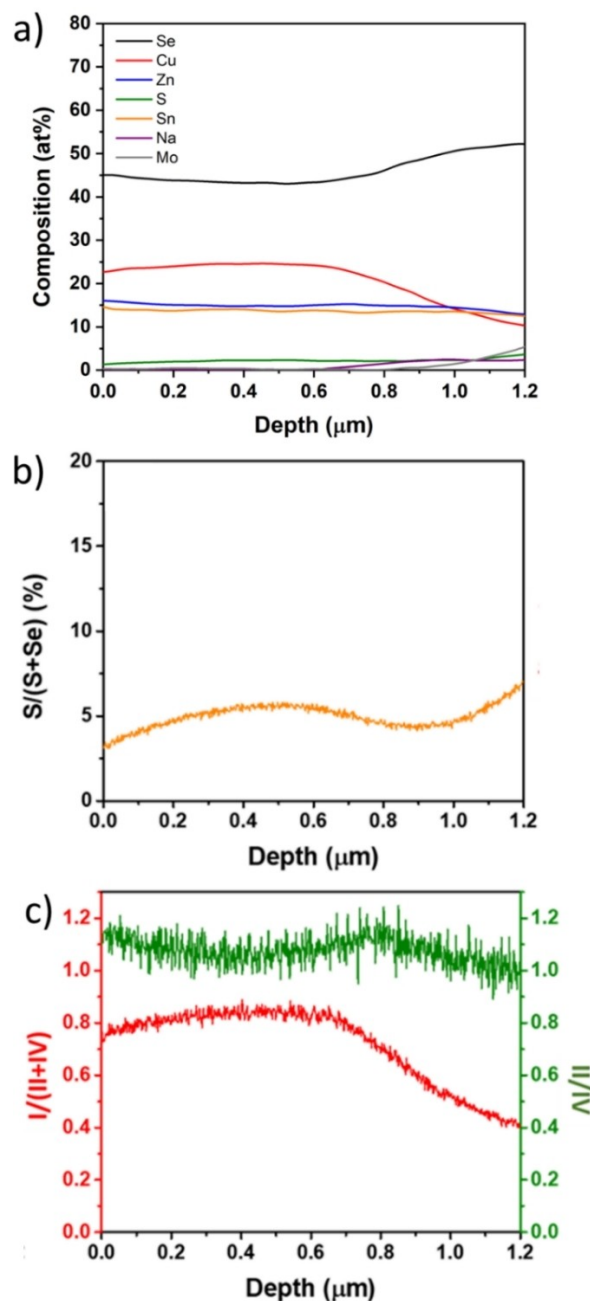


**Figure 1.** Depth elemental profile obtained by glow-discharge optical emission spectrometry (GDOES) of a) CZTSSe, b)  $S/(S+Se)$ , and c)  $I/(II+IV)$  and  $II/IV$  for the CZTSSe film deposited on Mo substrate.

illustrated in the grain size histogram shown in Figure 2b. Figure 2c shows the X-ray diffractograms of the CZTSSe films. These samples exhibit diffraction peaks at  $2\theta$  of around  $27.0^\circ$ ,  $48.0^\circ$ , and  $56.0^\circ$  which corresponds respectively to the (112), (204)/(220), and (312)/(116) planes of the tetragonal crystal structure (card No.:96-722-0527).<sup>[33,40]</sup> The absence of other diffraction peaks in XRD analysis than the peaks associated with the CZTSSe phase suggests that there are no significant impurity phases in the catalyst. Impurity phases such as  $SnSe_x$  may be present in Cu-poor and Zn-rich film compositions, yet detecting their diffraction peaks is difficult due to their

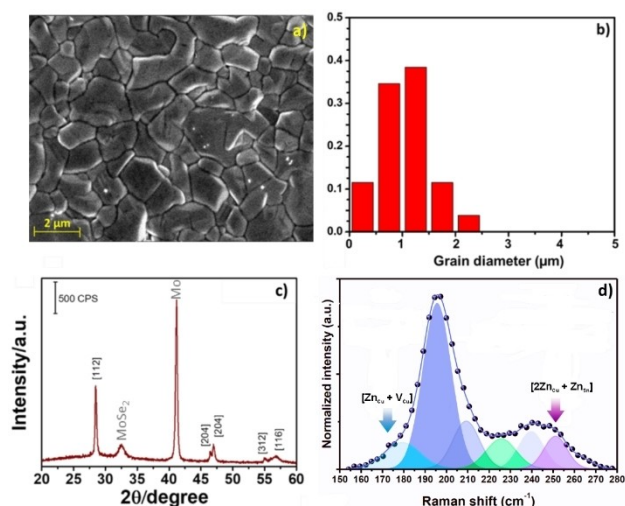


**Figure 2.** a) Surface SEM image, b) grain diameter histogram, c) XRD, and d) Deconvoluted Raman spectra of the CZTSSe film deposited on Mo substrate.

potentially low intensity resulting from a low concentration.<sup>[41]</sup> On the other hand, identifying a ZnSe secondary phase is challenging with XRD, as its diffraction peaks overlap with the main peaks of CZTSSe.<sup>[42]</sup> The diffraction peak at 42° corresponds to the Mo substrate, while the one at 33° indicates the formation of a MoSe<sub>2</sub> layer during selenization.<sup>[43]</sup>

The presence of defects in a crystalline material can induce local vibrational modes, resulting in the emergence of additional, typically subtle features in the Raman spectra. To investigate these effects, the Raman spectra were deconvoluted, specifically focusing on the peaks at 170 and 250 cm<sup>-1</sup>, as illustrated in Figure 2d. These peaks, respectively, are associated with the [Zn<sub>Cu</sub> + V<sub>Cu</sub>] and [2Zn<sub>Cu</sub> + Zn<sub>Sn</sub>] defect clusters. The creation of Zn<sub>Cu</sub> defects is accompanied by the formation of Sn<sub>Zn</sub> defects, this phenomenon contributes to stabilizing the coulombic charges within the lattice.<sup>[44]</sup>

The band gap energy ( $E_g$ ) of CZTSSe is the energy difference between the top of the valence band that is constituted by an antibonding linear combination of Cu-3d states and S-3p states and the bottom of the conduction band that is predominantly governed by an isolated band comprising of Sn-5s and S-3p states<sup>[45]</sup>. In this context, the optical band gap ( $E_g$ ) for CZTSSe was determined as 1.06 eV, in accordance with the literature,<sup>[33,46]</sup> using Tauc Plot, as illustrated in Figure 3a. The calculation of the absorption coefficient (Figure 3b) was performed using a model that includes sub-band gap states proposed by Katahara, presented in Equation (1)<sup>[47,48]</sup>:

$$\alpha(\varepsilon) = \frac{a_0 \sqrt{\gamma}}{2\Gamma(1 + \frac{1}{\theta})} \int_{-\infty}^{\Delta\varepsilon} \exp(-|\Delta\varepsilon'|^\theta) \sqrt{\Delta\varepsilon - \Delta\varepsilon'} [\Delta\varepsilon'] \quad (1)$$

The parameter  $a_0$  is specific to the material related to its oscillator strength;  $\gamma$  represents the broadening energy of the sub-bandgap absorption distribution, the Urbach energy;  $\theta$  determines the decay pattern of sub-bandgap states into the bandgap. For  $\theta$  values of 1, 1.25, 1.5, and 2, correspond to

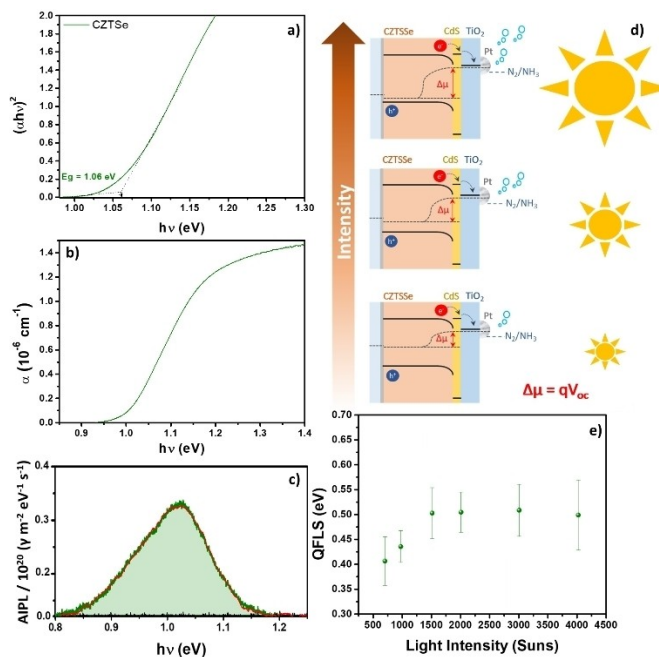


**Figure 3.** a) Tauc Plot for band gap energy determination, b) the absorption coefficient calculated from the Katahara's model, c) Absolute Intensity Photoluminescence, d) illustration of quasi-Fermi level pinning with light intensity, and e) QFLS vs. light intensity plot for the CZTSSe semiconductor.

Urbach, screened Thomas–Fermi with tunneling, Franz–Keldysh, and semiclassical Thomas–Fermi, respectively. The dimensionless energy parameter  $\Delta\varepsilon$  is defined as  $\Delta\varepsilon = (\varepsilon - E_g) / \gamma$ .  $\Gamma$  represents the conventional gamma function, defined as  $\Gamma(x) = (x-1)!$ , which is necessary for normalizing the integral over the sub-bandgap region of the function.<sup>[47,48]</sup> Katahara introduces a sub-bandgap absorption function characterized by two parameters,  $\gamma$  and  $\theta$ , which is integrated with a joint density-of-states model for direct band-to-band transitions within the effective mass approximation achieved through a convolutional integral, ensuring that the asymptotic properties of both the below and above bandgap models are maintained.<sup>[33]</sup>

This estimation relies on the absorption coefficient curves (inset of Figure 3a). In addition to  $E_g$ , the Urbach tail energy ( $E_u$ ) was also evaluated by examining the inverse of the slope of the linear portion of the  $\ln(\alpha)$  versus photon energy ( $h\nu$ ) plot.<sup>[49]</sup> The Urbach tail energy for the CZTSSe film was estimated at 29.8 meV. This  $E_u$  value, which surpasses the thermal energy ( $k_b T$ ), is attributed to the elevated density of I–II defects, leading to band tailing associated with the density of Zn<sub>Cu</sub> defects, in accordance with the Raman spectra.<sup>[50]</sup>

In this study, an analysis based on AIPL (Absolute Intensity Photoluminescence) was conducted to better understand the CZTSSe semiconductor properties. The AIPL spectra were fitted employing the photoluminescence model proposed by Katahara and Hillhouse,<sup>[51]</sup> designed for semiconductors with direct electronic transition obtained with a 780 nm excitation for CZTSSe (Figure 3c). This fitting process facilitated the determi-

nation of the direct bandgap ( $E_g$ ), which was 1.01 eV, close to the value determined by Tauc plot.

Besides  $E_g$ , the AIPL fitting permitted the determination of the quasi-Fermi level splitting (QFLS), which is a direct measure of the open circuit voltage ( $V_{oc}$ ) in solar cells or the photovoltage ( $V_{ph}$ ) in photoelectrochemical systems. For CZTSSe produced in this work, the QFLS was estimated at 0.40 eV, in accordance with the literature.<sup>[52,53]</sup>

Analysis of light intensity versus open-circuit voltage ( $V_{oc}$ ) is a common approach for determining Fermi-level pinning in photovoltaic devices, as illustrated in Figure 3d. Similarly, AIPL spectra were obtained under varying light intensities (data not shown), and fitting the model for each spectrum, the quasi-Fermi level splitting (QFLS) was determined, and the resulting QFLS versus light intensity plot is presented in Figure 3e. The plot reveals an increase in QFLS with light intensity up to 1500 Suns, after which it becomes pinned at higher intensities. This pinning of QFLS occurs at 0.51 eV. Notably, this QFLS pinning is less pronounced than observed in Ag-doped CZTSSe (ACZTSSe) films.<sup>[33]</sup> Since Ag doping is known to suppress defects, this indicates that the low pinning of QFLS of the CZTSSe is due to mid-gap states raised from defects and band tailing. This result aligns with the Urbach energy value and Raman analysis.

## N<sub>2</sub> Reduction Reaction

The photoelectrochemical properties of the kesterite-based photocathodes were characterized using linear sweep voltammetry (LSV) under transient light incidence for the catalyst without (Figure 4a) and with Pt decoration on the catalyst surface (Figure 4b) and with and without light incidence comparing the photocurrent response obtained under support-

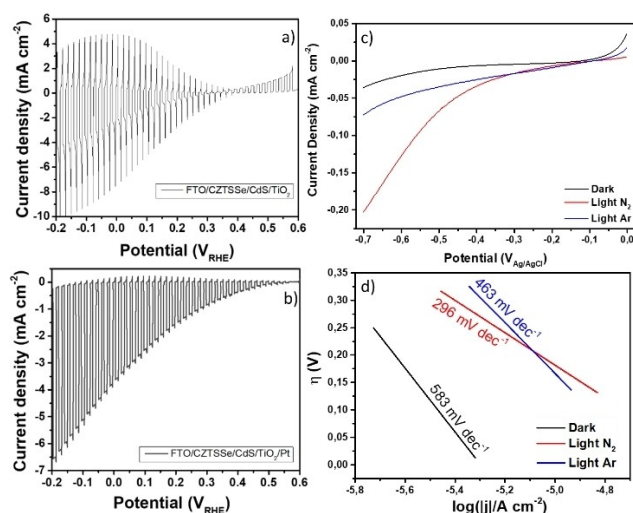


**Figure 4.** Linear sweep voltammetry (LSV) curves in a 1.0 mol L<sup>-1</sup> H<sub>2</sub>SO<sub>4</sub> solution (pH 0.4) at 10 mVs<sup>-1</sup>, under chopped simulated sunlight (AM 1.5 G filter and 100 mWcm<sup>-2</sup> of a) CZTSSe/CdS/TiO<sub>2</sub> and b) CZTSSe/CdS/TiO<sub>2</sub>/Pt, and c) LSV for the CZTSSe/CdS/TiO<sub>2</sub>-Pt photocathode in 0.1 mol L<sup>-1</sup> Na<sub>2</sub>SO<sub>3</sub> supporting electrolyte saturated with N<sub>2</sub> under dark (black curve) and 1 sun of light incidence (red curve), and under 1 sun of light incidence in the supporting electrolyte saturated with Ar (blue curve).

ing electrolyte purged with nitrogen (N<sub>2</sub>) and with argon (Ar) (Figure 4c). The Tafel plot obtained from the LSV under dark and light with the supporting electrolyte saturated with N<sub>2</sub> and Ar (Figure 4c) is presented in Figure 4d.

The chopped illumination contributes to inferring the charge separation and recombination of carriers at the surface of the photocatalyst. The immediate rise in photocurrent upon activating the light corresponds to the fast separation of electron-hole pairs generated within the space charge region, the so-called "on spike".<sup>[54]</sup> The subsequent decline in photocurrent is ascribed to the accumulation of minority carriers (in the case of p-type semiconductors, electrons) near the interface, leading to an increase of holes in the surface due to recombination (decreasing the nominal value of the current).<sup>[55]</sup> The CZTSSe/CdS/TiO<sub>2</sub> photocatalyst (Figure 4a) presents a short rise time of the on spike, indicating a fast separation of the carrier under light incidence. Over time, a stable state is achieved where the rate of electrons reaching the interface equals the rate at which they are utilized in charge transfer and recombination.<sup>[38,54]</sup> As a result, the photocurrent levels off, maintaining a constant value equivalent to the current passing through the semiconductor/electrolyte interface. The photocatalyst also presents an overshoot well pronounced, which is the spike formed in the positive region of current when the light is switched off, due to the interruption on the electrons flux, leaving just the hole flux, which, as in the opposite case, decays until the recombination and charge transfer processes have fully consumed all excess of holes, making the current to reach zero again. However, this short rise time of the on spike presents a significant decay in the photocurrent density after potentials below 0.35 V<sub>RHE</sub>, and this behavior increases with the decrease of the potential, indicating a high recombination of electrons and holes just after its photoexcitation, mainly in potentials where the N<sub>2</sub>RR is more likely to happen. Additionally, this photocatalyst presents a mix of characteristics, behaving as n-type and p-type semiconductors depending on the potential applied to the system (related to RHE).

After the decoration of the CZTSSe/CdS/TiO<sub>2</sub> photocatalyst surface with Pt nanoparticles the transient photocurrent response of the semiconductor changed completely (Figure 4b). Despite the short rise time of the on-spike, the decay decreased considerably and there is no overshoot under negative potentials. It leads to the conclusion that the presence of Pt nanoparticles on the catalyst surface does not interfere in the separation of the photogenerated carriers, however, it improves the charge transfer decreasing the recombination rate. That modification entailed a higher photocurrent density value in the stable state and brought a p-type characteristic for the photocatalyst in the potential region investigated.

To evaluate the behavior of the CZTSSe/CdS/TiO<sub>2</sub>-Pt photocathode for the N<sub>2</sub> reduction reaction LSV was conducted in the absence of light and under irradiation using a solar simulator (100 mWcm<sup>-2</sup> with AM 1.5 G filter) in a saturated supporting electrolyte with argon (Ar) and with nitrogen (N<sub>2</sub>) gas (Figure 4c). A comparison of the curves under light and dark conditions revealed an increase in cathodic current when the semiconductor was illuminated under the electrolyte saturated

with Ar or N<sub>2</sub>. The increase in cathodic current under light exposure can be explained by the generation of electron/hole pairs (e<sup>-</sup>/h<sup>+</sup>) through the absorption of photons with energy equal to or greater than the semiconductor's band gap.<sup>[56,57]</sup> However, when the supporting electrolyte was saturated with N<sub>2</sub>(g) instead of Ar(g), an even higher photocurrent density was observed, showing that under the same conditions, more electrons were transferred from the CZTSSe/CdS/TiO<sub>2</sub>-Pt photocatalyst surface to the N<sub>2</sub> molecule in detrimental to the Ar-saturated reaction system, mainly under potentials below -0.35 V<sub>Ag/AgCl</sub>, indicating a greater propensity of the catalyst to reduce N<sub>2</sub>.

One of the main parameters obtained in this thermodynamic-kinetics analysis is the Tafel slope, which indicates the minimal potential required to increase the density current in one decade. In this sense, both dark and light conditions with Ar gas resulted in the biggest Tafel slopes of 583 mVdec<sup>-1</sup> and 463 mVdec<sup>-1</sup>, respectively. On the other hand, the minimal slope value of 296 mVdec<sup>-1</sup> was verified for the illuminated photocathode saturated with N<sub>2</sub>, indicating in this last case the lowest energy needed for the N<sub>2</sub>RR occurs, reflecting the optimized conditions for NH<sub>3</sub> synthesis using the CZTSSe/CdS/TiO<sub>2</sub>-Pt photocathode. A lower Tafel slope suggests the system is more energy-efficient and has better electrochemical kinetics.

As the photocatalyst showed to have a good photoresponse under an N<sub>2</sub>-saturated reaction system, the N<sub>2</sub> reduction reaction was investigated chronoamperometry technique for 120 min under different applied potential and light irradiation using a solar simulator (100 mWcm<sup>-2</sup> with AM 1.5 G filter) in a saturated supporting electrolyte N<sub>2</sub> gas (Figure 5a). The quantification of NH<sub>3</sub> was performed by a fast and simple colorimetric method widely used in this reaction and already discussed in companion work.<sup>[55]</sup> It is already well known that the N<sub>2</sub>RR

occurs under low bias potential if the activation of the semiconductor is based on the light incidence.<sup>[58-60]</sup> Taking into consideration that the OCP of the material after light incidence was close to -0.2 V<sub>Ag/AgCl</sub>, the N<sub>2</sub>RR was investigated from -0.2 to -0.6 V<sub>Ag/AgCl</sub>. The best potential to drive the N<sub>2</sub>RR to a higher NH<sub>3</sub> formation using the semiconductor decorated with Pt nanoparticles was -0.4 V<sub>Ag/AgCl</sub> using 0.1 molL<sup>-1</sup> Na<sub>2</sub>SO<sub>3</sub> constantly saturated with N<sub>2</sub> as supporting electrolyte, reaching 0.22 mmolL<sup>-1</sup> cm<sup>-2</sup> NH<sub>3</sub>.

In this process, the photons with energy greater than the band gap of the semiconductor generate the electron-hole pairs (e<sup>-</sup>/h<sup>+</sup> charge carriers) responsible for the reduction of N<sub>2</sub> to the N<sub>2</sub> radical (N<sub>2</sub><sup>•-</sup>) as observed in reaction 1.<sup>[61]</sup> The hydrogen necessary for the NH<sub>3</sub> formation is generated from the oxidation of water from the holes (reaction 2) formed during the excitation of the electrons from the valence band to the conduction band.<sup>[62]</sup> The reaction between those H<sup>+</sup> and N<sub>2</sub><sup>•-</sup> produces the ammonium (reaction 3).<sup>[55]</sup> Even though the photons incidence is responsible for the charge carrier generation, the applied potential in the photoelectrocatalysis technique assures the maximum separation of those charges avoiding the recombination along the reaction steps.



After evaluating the best applied potential for the NH<sub>3</sub> formation, the type of the supporting electrolyte was investigated (Figure 5b) together with a variation in its pH based on the more employed solutions for reduction reactions in the literature.<sup>[32,63-65]</sup> It can influence the yields in electrosynthesis reactions, once the supporting electrolyte is evolved in the interface of the charge carriers transfer among the photocatalyst and the reactional species.<sup>[66,67]</sup> The variation in the pH value does not present a great signification in the NH<sub>3</sub> generation, in contrast with what occurs for the CO<sub>2</sub> reduction reaction.<sup>[68,69]</sup> On the other hand, the supporting electrolyte type seems to be the key to improving the ammonium synthesis, without excluding the importance of the photocatalyst. In this case, Na<sub>2</sub>SO<sub>3</sub> acts as a sacrificial reagent consuming the holes and generating Na<sub>2</sub>SO<sub>4</sub> in the reaction solution.<sup>[64,70]</sup> The consumption of the photogenerated holes is probably the reason for the improvement in the ammonium generation, once it prevents the oxidation of the generated product.

The best condition for the N<sub>2</sub>RR under PEC was also applied using the photocatalysis technique (PC, without bias potential), electrocatalysis technique (EC, without light incidence), and PEC for the semiconductor without Pt nanoparticles decoration as control experiments (Figure 5c). It is evident that the photocatalyst needs the combination of both, the bias potential, and the photons incidence to achieve better performance. The necessity of the Pt nanoparticles has been presented and discussed previously (Figure 4b) and confirmed concerning the

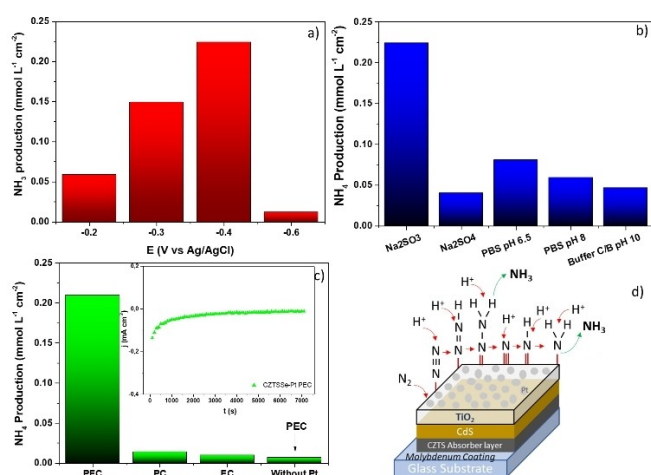


**Figure 5.** NH<sub>3</sub> photoelectrosynthesis from N<sub>2</sub> reduction reaction using CZTSSe/CdS/TiO<sub>2</sub>-Pt photocathode and 0.05 molL<sup>-1</sup> H<sub>2</sub>SO<sub>4</sub> as supporting electrolyte in anodic chamber, under 1 sun of light incidence and a) different applied potential under 0.1 molL<sup>-1</sup> Na<sub>2</sub>SO<sub>3</sub> supporting electrolyte in the cathodic chamber, b) different supporting electrolyte in the cathodic side and applying -0.4 V<sub>Ag/AgCl</sub>, c) different techniques under -0.4 V<sub>Ag/AgCl</sub>, except for PC, and the best condition for the CZTSSe/CdS/TiO<sub>2</sub> photocathode with the inset showing the stability of the catalyst over 7200s of PEC, and d) schematic representation of the NH<sub>3</sub> formation pathway.

NH<sub>3</sub> production (Figure 5c). Additionally, the stability of the photocatalyst is demonstrated in the inset of Figure 5c, where can be observed a photocurrent density of over 7200s under PEC reaction of N<sub>2</sub> reduction without a significant variation in the photocurrent along the time.

The associative pathway, which is one of the possibilities for NH<sub>3</sub> formation is presented in Figure 5d. As demonstrated in this representative scheme in the associative mechanism, both N atoms stay bonded to each other as hydrogenation takes place until an NH<sub>3</sub> molecule is formed, at which point the last N–N bond is disrupted.<sup>[71]</sup> It is noteworthy to highlight that in this scenario, hydrogenation can occur preferentially through a distal associative pathway, where hydrogen is inserted into the external N first, as illustrated in Figure 5d. Alternatively, it can follow an associative alternating pathway, where the addition of H alternates between each of the two nitrogen centers.<sup>[61]</sup>

## Conclusions

The CZTSSe thin films were prepared by an easy solution-processed deposition method with the composition obtained with no detected secondary phases. The photocurrent behavior of the chalcopyrite-based photocathodes drove the choice of the photoelectrodeposition of Pt nanoparticles on the semiconductor surface acting as cocatalysts. This modification proves to be exceptionally effective in converting solar energy into ammonia through an N<sub>2</sub> reduction reaction. This efficacy is attributed to the renowned high activity of noble metals, such as Pt, in facilitating the catalytic reaction. An investigation around the supporting electrolyte type showed that the Na<sub>2</sub>SO<sub>3</sub> is the more indicated option for a high yield of NH<sub>3</sub> formation, probably because it acts as a sacrificial agent avoiding product oxidation. Lastly, as expected, the photoelectrocatalysis technique turned out to be the best approach to promote the photoelectrosynthesis of ammonia under ambient conditions when compared to photocatalysis and electrocatalysis techniques.

## Experimental Section

### Chemical Reagents

All the chemicals were purchased from Sigma-Aldrich with the following purity, N,N-anhydrous dimethylformamide (DMF) (99.98%), Cu(CH<sub>3</sub>CO<sub>2</sub>H)<sub>2</sub> (99.99%), ZnCl<sub>2</sub> (99.99%), SnCl<sub>2</sub> (99.99%), thiourea (TU, 99.0%), H<sub>2</sub>PtCl<sub>6</sub> (99.9%), Na<sub>2</sub>SO<sub>4</sub> (99.0%), Na<sub>2</sub>SO<sub>3</sub> (99.0%), H<sub>2</sub>SO<sub>4</sub> (98.0%), Na<sub>2</sub>CO<sub>3</sub> (99.5%) NaHCO<sub>3</sub> (99.5%), NaH<sub>2</sub>PO<sub>4</sub> (99.0%), NaCl (99.5%) and H<sub>3</sub>PO<sub>4</sub> (99.0%).

### Photocathode Synthesis

The kesterite films were deposited on the fluorine-doped tin oxide surface (FTO, 7 ohm/sq, MTI corporation) by spin coating under 3000 rpm and 60 s. According to the literature,<sup>[72]</sup> the FTO was cleaned and hydrophilized before its use. The CZTS molecular ink was prepared by 5 mol L<sup>-1</sup> thiourea, de 0.53 mol L<sup>-1</sup> Cu(CH<sub>3</sub>CO<sub>2</sub>H)<sub>2</sub>, 0.87 mol L<sup>-1</sup> ZnCl<sub>2</sub>, 0.83 mol L<sup>-1</sup> SnCl<sub>2</sub> and 0.03 LiCl diluted in DMF,

based on the literature.<sup>[33,73]</sup> Elemental ratios were Cu/(Zn + Sn) = 0.75 and Zn/Sn = 1.05, to obtain a Cu-poor and Zn-rich CZTSSe composition. All solutions were prepared at room temperature in an N<sub>2</sub>-filled glovebox with O<sub>2</sub> and H<sub>2</sub>O concentrations controlled below 20 ppm. After the deposition, the films were heated in the heating plate at 270 °C for 90 s. The Se insertion was made by thermal treatment of the as-prepared CZTS under Se atmosphere (selenization) at 550 °C for 20 min. The CdS layer was inserted on the CZTSSe surface by chemical bath deposition (CBD) for 8.50 min at 65 °C, in a solution composed of 150 mL of deionized water, 22 mL of 0.015 mol L<sup>-1</sup> CdSO<sub>4</sub> solution, 22 mL of 0.75 mol L<sup>-1</sup> thiourea solution, and 28 mL of NH<sub>4</sub>OH 30%. After the CBD the CZTSSe/CdS films were washed with ultrapure water and dried with N<sub>2</sub> gas to the deposition of the TiO<sub>2</sub> layer. The TiO<sub>2</sub> layer deposition was performed by spin coating under 3000 rpm and 60 s using 400 μL of 20% (v/v) titanium isopropoxide in an isopropanol solution. After the deposition, the films were heated in a heating plate at 200 °C for 30 min. The Pt photoelectrodeposition (PED) was performed according to Tinoco and coworkers<sup>[38]</sup> in a one-compartment three-electrode cell with Pt wire as auxiliary electrode and Ag/AgCl/Cl<sup>-</sup> (sat. KCl) as reference electrode, using a pH 6.5 solution as supporting electrolyte composed by 1.0 mmol L<sup>-1</sup> H<sub>2</sub>PtCl<sub>6</sub> in 0.1 mol L<sup>-1</sup> phosphate buffer and 0.5 mol L<sup>-1</sup> Na<sub>2</sub>SO<sub>4</sub> and applying -0.1 V<sub>Ag/AgCl</sub> for 10 min under 1 sun illumination (solar simulator with a 100 W Xe lamp and an AM 1.5 G filter, Oriel, LSC-100). A scheme of all steps to perform the electrocatalyst synthesis is represented in the scheme present in Figure 6.

### Photocathode Characterization

The structure, morphology, and composition of the CZTSSe/CdS/TiO<sub>2</sub> photocathode decorated with Pt were characterized using Glow-Discharge Optical Emission Spectrometry (GDOES, Horiba GD-Profilier 2), Scanning Electron Microscopy (SEM, FEI Sirion XL30 microscope), X-Ray Diffraction (XRD, Bruker D8 Discover diffractometer), Energy-dispersive X-ray spectroscopy analysis (EDS, Oxford EDX detector using an accelerating voltage of 20 kV) and Raman spectroscopy (Micro Raman spectrophotometer, Horiba iHR-550). The transmittance of the films was acquired between 500–2200 nm using a UV-Vis-NIR spectrophotometer Perkin Elmer Lambda 1050 equipped with a Peltier-cooled InGaAs detector for IR, PbS detector for the NIR, and a tungsten-halogen lamp as an emission source. Absolute Intensity Photoluminescence (AIPL) spectra were collected using a calibrated confocal modified Horiba LabRAM HR-800 with a 785 nm laser as an excitation source. The adjustable confocal hole before the monochromator was set at 800 μm, and a 10x objective was used. A 150 grooves/mm Czerny-Turner monochromator blazed at 1200 nm was used, and the emitted light was passed to a InGaAs array detector cooled with liquid nitrogen. The system was continually purged with dry air to remove unwanted effects from the water in the produced spectra. To obtain the quasi-Fermi level splitting (QFLS), the AIPL spectra were obtained under varying light

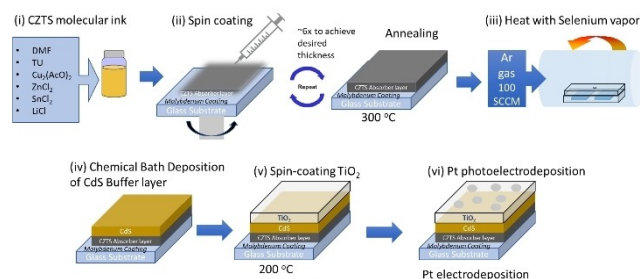


Figure 6. Representative scheme of the photocathode thin film synthesis.

intensities, and the QFLS for each spectrum was determined by fitting the model and plotting the resulting QFLS versus light intensity. The transmittance of the films was acquired between 500–2200 nm using a UV-Vis-NIR spectrophotometer Perkin Elmer Lambda 1050 equipped with a Peltier-cooled InGaAs detector for IR, PbS detector for the NIR, and a tungsten-halogen lamp as an emission source. Photocurrent measurements were performed with linear sweep voltammograms, measured at  $10 \text{ mVs}^{-1}$ , using a 150 W commercial solar simulator lamp (Oriol – LSC-100) with an intensity of  $100 \text{ mWcm}^{-2}$  (1 sun, calibrated with a power and energy meter, Thorlabs) at standard conditions ( $25^\circ\text{C}$  and AM1.5 G) and a potentiostat/galvanostat (Autolab model PGSTAT 302, Metrohm).

## N<sub>2</sub> Reduction Reaction

The N<sub>2</sub> reduction reaction procedure was adapted from Brito and coworkers.<sup>[55]</sup> The photoelectrocatalytic reduction of N<sub>2</sub> was performed in a completely sealed H-cell with three electrodes with anodic and cathodic chambers separated by a proton exchange membrane (PEM) Nafion™, a cooling system, and a quartz window. An Ag/AgCl/Cl<sup>-</sup> (3.0 M KCl) electrode was used as the reference electrode and a Pt plate as the counter electrode. The reaction was carried out in different supporting electrolytes such as Na<sub>2</sub>SO<sub>4</sub>, Na<sub>2</sub>SO<sub>3</sub>, PBS, and carbonate/bicarbonate buffer, all of them with a concentration of  $0.1 \text{ molL}^{-1}$  saturated with N<sub>2</sub> gas that was bubbled throughout the entire experiment for the cathodic compartment. H<sub>2</sub>SO<sub>4</sub>  $0.05 \text{ molL}^{-1}$  was applied as a supporting electrolyte in the anodic compartment. A 30 mL acid trap of  $0.005 \text{ molL}^{-1}$  H<sub>3</sub>PO<sub>4</sub><sup>[74]</sup> was connected to the cathodic compartment for ammonia to be collected during the reaction. Photoelectrocatalysis was performed under different potentials with the 1 sunlight irradiation (Xe lamp and AM 1.5 G filter, Oriol – LSC-100,  $100 \text{ mWcm}^{-2}$ ) for the CZTSSe/CdS/TiO<sub>2</sub> photocathode with and without Pt. Aliquots were collected after 2 h of reaction and the amount of NH<sub>3</sub> was analyzed by a colorimetric method of indophenol blue using the Merck Spectroquant® commercial kit.

## Acknowledgements

The authors thank the Laboratory of Structural Characterization, LCE/DEMa/UFSCar, for general facilities.

Funding: This work was supported by the Serrapilheira Institute [Grant number Serra – 2211-41925]; São Paulo Research Foundation, FAPESP [Grant numbers #2023/10027-5, #2023/14228-5, #2019/26860-2, #2018/02950-0, #2017/12794-2, #2018/26005-2, #2018/16401-8 and #2014/50249-8]; Conselho Nacional de Desenvolvimento Científico e Tecnológico, CNPq [Grant number #152471/2018-9, #406156/2022-0]; Coordenação de Aperfeiçoamento de Pessoal de Nível Superior – Brasil, CAPES [Grant number 001]; and INCT-DATREM [Grant number #465571/2014-0].

## Conflict of Interests

The authors declare no conflict of interest.

## Data Availability Statement

The data that support the findings of this study are available from the corresponding author upon reasonable request.

**Keywords:** CZTSSe semiconductor · Ammonia production · Photoelectrochemical process · Thin films

- [1] B. Wang, T. Li, F. Gong, M. H. D. Othman, R. Xiao, *Fuel Process. Technol.* **2022**, *235*, 107380.
- [2] D. Saygin, H. Blanco, F. Boshell, J. Cordonnier, K. Rouwenhorst, P. Lathwal, D. Gielen, *Sustainability* **2023**, *15*(2), 1623.
- [3] M. Aziz, A. TriWijayanta, A. B. D. Nandiyanto, *Energies (Basel)* **2020**, *13*(12), 1.
- [4] J. Humphreys, R. Lan, S. Tao, *Adv. Energy Sustainability Res.* **2021**, *2*, 1.
- [5] J. Humphreys, R. Lan, S. Tao, *Adv. Energy Sustainability Res.* **2021**, *2*, 1.
- [6] L. Wang, X. Yan, W. Si, D. Liu, X. Hou, D. Li, F. Hou, S. X. Dou, J. Liang, *Chin. J. Catal.* **2022**, *43*(7), 1761.
- [7] X. Cui, C. Tang, Q. Zhang, *Adv. Energy Mater* **2018**, *8*(22), 1800369.
- [8] Z. Yan, M. Ji, J. Xia, H. Zhu, *Adv. Energy Mater* **2020**, *10*(11), 1.
- [9] D. Yuan, Z. Wei, P. Han, C. Yang, L. Huang, Z. Gu, Y. Ding, J. Ma, G. Zheng, *J. Mater. Chem. A Mater.* **2019**, *7*(28), 16979.
- [10] Y. Zhao, L. Yan, X. Zhao, *ChemElectroChem* **2022**, *9*, 3.
- [11] D. Liu, J. Wang, S. Bian, Q. Liu, Y. Gao, X. Wang, P. K. Chu, X. F. Yu, *Adv. Funct. Mater* **2020**, *30*, 24.
- [12] J. Nash, X. Yang, J. Anibal, J. Wang, Y. Yan, B. Xu, *J. Electrochem. Soc.* **2017**, *164*(14), F1712.
- [13] Y. Wang, A. Xu, Z. Wang, L. Huang, J. Li, F. Li, J. Wicks, M. Luo, D. H. Nam, C. S. Tan, Y. Ding, J. Wu, Y. Lum, C. T. Dinh, D. Sinton, G. Zheng, E. H. Sargent, *J. Am. Chem. Soc.* **2020**, *142*(12), 5702.
- [14] Y. Liu, B. Deng, K. Li, H. Wang, Y. Sun, F. Dong, *J. Colloid Interface Sci.* **2022**, *614*, 405.
- [15] L. Zhang, X. Ji, X. Ren, Y. Ma, X. Shi, Z. Tian, A. M. Asiri, L. Chen, B. Tang, X. Sun, *Adv. Mater.* **2018**, *30*(28), 2.
- [16] Y. Guo, Z. Yao, B. J. J. Timmer, X. Sheng, L. Fan, Y. Li, F. Zhang, L. Sun, *Nano Energy* **2019**, *62*, 282.
- [17] B. Liu, C. Ma, D. Liu, S. Yan, *ChemElectroChem* **2021**, *8*(16), 3030.
- [18] R. Zhao, Y. Chen, H. Xiang, Y. Guan, C. Yang, Q. Zhang, Y. Li, Y. Cong, X. Li, *ACS Appl. Mater. Interfaces* **2023**, *15*(5), 6797.
- [19] J. Kong, A. Lim, C. Yoon, J. H. Jang, H. C. Ham, J. Han, S. Nam, D. Kim, Y. E. Sung, J. Choi, H. S. Park, *ACS Sustain. Chem. Eng.* **2017**, *5*(11), 10986.
- [20] Y. Li, Y. Liu, X. Liu, Y. Liu, Y. Cheng, P. Zhang, P. Deng, J. Deng, Z. Kang, H. Li, *Nano Research.* **2022**, *15*(7), 6026.
- [21] J. Zheng, L. Jiang, Y. Lyu, S. P. Jiang, S. Wang, *Energy Environ. Mater.* **2022**, *5*(2), 452.
- [22] C. Choi, G. H. Gu, J. Noh, H. S. Park, Y. Jung, *Nat. Commun.* **2021**, *12*(1), 1.
- [23] H. Wang, C. Cheng, K. Du, Z. Xu, E. Zhao, N. Lan, P. F. Yin, T. Ling, *Chem. – A Eur. J.* **2023**, *29*(25), 1.
- [24] L. Li, C. Tang, B. Xia, H. Jin, Y. Zheng, S. Z. Qiao, *ACS Catal.* **2019**, *9*(4), 2902.
- [25] N. Dilshod, K. Kholmirzo, S. Aliona, F. Kahramon, G. Viktoriya, K. Tamerlan, B.-J. Potential, *Lett. Appl. NanoBioSci.* **2022**, *12*(3), 67.
- [26] S. Grau, S. Giraldo, E. Saucedo, J. R. Morante, A. Llobet, C. Gimbert-Suriñach, *J. Mater. Chem. A Mater.* **2019**, *7*(42), 24320.
- [27] J. Li, D. Wang, X. Li, Y. Zeng, Y. Zhang, *Adv. Sci. (Weinh)* **2018**, *5*, 4.
- [28] O. Gunawan, T. Gokmen, D. B. Mitzi, *J. Appl. Phys.* **2014**, *116*, 8.
- [29] Y. Qi, Q. Tian, Y. Meng, D. Kou, Z. Zhou, W. Zhou, S. Wu, *ACS Appl. Mater. Interfaces* **2017**, *9*(25), 21243.
- [30] M. B. Costa, F. W. S. Lucas, M. Medina, L. H. Mascaró, *ACS Appl. Energy Mater* **2020**, *3*(10), 9799.
- [31] P. Lianos, *Appl. Catal. B* **2017**, *210*(5), 235.
- [32] S. F. Blaskiewicz, I. Freitas Teixeira, L. H. Mascaró, J. Ferreira de Brito, *ChemCatChem* **2023**, *15*, 5.
- [33] M. dos S. Araujo, H. L. S. dos Santos, M. Medina, A. C. Salomao, L. H. Mascaró, M. A. S. Andrade, *Electrochim. Acta* **2023**, *464*, 142935.
- [34] C. Yan, J. Huang, K. Sun, S. Johnston, Y. Zhang, H. Sun, A. Pu, M. He, F. Liu, K. Eder, L. Yang, J. M. Cairney, N. J. Ekins-Daukes, Z. Hameiri, J. A. Stride, S. Chen, M. A. Green, X. Hao, *Nat. Energy* **2018**, *3*(9), 764.
- [35] S. Zhou, K. Sun, C. Y. Toe, J. Yin, J. Huang, Y. Zeng, D. Zhang, W. Chen, O. F. Mohammed, X. Hao, R. Amal, *Adv. Mater.* **2022**, *34*, 29.
- [36] C. Ding, J. Shi, Z. Wang, C. Li, *ACS Catal.* **2017**, *7*(1), 675.

- [37] J. Tan, W. Yang, Y. Oh, H. Lee, J. Park, J. Moon, *ACS Appl. Mater. Interfaces* **2018**, *10*(13), 10898.
- [38] M. V. de L. Tinoco, M. B. Costa, L. H. Mascaro, J. F. de Brito, *Electrochim. Acta* **2021**, *382*, 138290.
- [39] J. Park, H. Yoo, V. Karade, K. S. Gour, E. Choi, M. Kim, X. Hao, S. J. Shin, J. Kim, H. Shim, D. Kim, J. H. Kim, J. Yun, J. H. Kim, *J. Mater. Chem. A Mater.* **2020**, *8*(29), 14538.
- [40] J. Li, S. Y. Kim, D. Nam, X. Liu, J. H. Kim, H. Cheong, W. Liu, H. Li, Y. Sun, Y. Zhang, *Sol. Energy Mater. Sol. Cells* **2017**, *159*, 447.
- [41] M. Dimitrievska, A. Fairbrother, E. Saucedo, A. Pérez-Rodríguez, V. Izquierdo-Roca, *Sol. Energy Mater. Sol. Cells* **2016**, *149*, 304.
- [42] J. Just, C. M. Sutter-Fella, D. Lützenkirchen-Hecht, R. Frahm, S. Schorr, T. Unold, *Phys. Chem. Chem. Phys.* **2016**, *18*(23), 15988.
- [43] L. Yao, J. Ao, M. J. Jeng, J. Bi, S. Gao, G. Sun, Q. He, Z. Zhou, Y. Sun, L. B. Chang, *Sol. Energy Mater. Sol. Cells* **2017**, *159*, 318.
- [44] M. Dimitrievska, F. Oliva, M. Guc, S. Giraldo, E. Saucedo, A. Pérez-Rodríguez, V. Izquierdo-Roca, *J. Mater. Chem. A Mater.* **2019**, *7*(21), 13293.
- [45] J. Paier, R. Asahi, A. Nagoya, G. Kresse, *Phys. Rev. B Condens. Matter. Mater. Phys.* **2009**, *79*, 11.
- [46] A. Fairbrother, E. García-Hemme, V. Izquierdo-Roca, X. Fontané, F. A. Pulgarín-Agudelo, O. Vigil-Galán, A. Pérez-Rodríguez, E. Saucedo, *J. Am. Chem. Soc.* **2012**, *134*(19), 8018.
- [47] I. L. Braly, R. J. Stoddard, A. Rajagopal, A. K. Y. Jen, H. W. Hillhouse, *J. Phys. Chem. Lett.* **2018**, *9*(13), 3779.
- [48] R. J. Stoddard, F. T. Eickemeyer, J. K. Katahara, H. W. Hillhouse, *J. Phys. Chem. Lett.* **2017**, *8*(14), 3289.
- [49] J. Chantana, Y. Kawano, T. Nishimura, A. Mavlonov, T. Minemoto, *Sol. Energy Mater. Sol. Cells* **2020**, *210*, 110502.
- [50] W. C. Huang, S. Y. Wei, C. H. Cai, W. H. Ho, C. H. Lai, *J. Mater. Chem. A Mater.* **2018**, *6*(31), 15170.
- [51] J. K. Katahara, H. W. Hillhouse, *J. Appl. Phys.* **2014**, *116*, 17.
- [52] A. Redinger, T. Unold, *Sci. Rep.* **2018**, *8*, 1.
- [53] M. Azzouzi, A. Cabas-Vidani, S. G. Haass, J. A. Röhr, Y. E. Romanyuk, A. N. Tiwari, J. Nelson, *J. Phys. Chem. Lett.* **2019**, 2829.
- [54] L. M. Peter, A. B. Walker, T. Bein, A. G. Hufnagel, I. Kondofersky, *J. Electroanal. Chem.* **2020**, *872*, 114234.
- [55] J. F. de Brito, M. B. Costa, K. Rajeshwar, L. H. Mascaro, *Electrochim. Acta* **2022**, *421*, 140475.
- [56] G. G. Bessegato, T. T. Guaraldo, J. F. de Brito, M. F. Brugnera, M. V. B. Zanoni, *Electrocatalysis* **2015**, *6*(5), 415.
- [57] E. Zarei, R. Ojani, *J. Solid State Electrochem.* **2017**, *21*(2), 305.
- [58] L. P. Camargo, P. R. C. da Silva, A. Batagin-Neto, V. Klobukoski, M. Vidotti, L. H. Dall'Antonia, *Appl. Mater. Today* **2022**, *28*, 101540.
- [59] M. A. Mushtaq, M. Arif, X. Fang, G. Yasin, W. Ye, M. Basharat, B. Zhou, S. Yang, S. Ji, D. Yan, *J. Mater. Chem. A Mater.* **2021**, *9*(5), 2742.
- [60] Y. Bai, J. Lu, H. Bai, Z. Fang, F. Wang, Y. Liu, D. Sun, B. Luo, W. Fan, W. Shi, *Chem. Eng. J.* **2021**, *414*, 128773.
- [61] M. A. Shipman, M. D. Symes, *Catal. Today* **2017**, *286*, 57.
- [62] J. F. Brito, G. G. Bessegato, P. R. F. de T. Souza, T. S. Viana, D. P. Oliveira, C. A. Martínez-huitle, M. V. B. Zanoni, *J. Electrochem. Soc.* **2019**, *166*(5), 3231.
- [63] J. F. de Brito, M. A. S. Andrade, M. V. B. Zanoni, L. H. Mascaro, *J. CO2 Util.* **2022**, *57*, 101902.
- [64] M. Ali, F. Zhou, K. Chen, C. Kotzur, C. Xiao, L. Bourgeois, X. Zhang, D. R. MacFarlane, *Nat. Commun.* **2016**, *7*, 11335.
- [65] J. F. Brito, A. A. Silva, A. J. Cavalheiro, M. V. B. Zanoni, *Int. J. Electrochem. Sci.* **2014**, *9*(11), 5961.
- [66] J. F. de Brito, G. G. Bessegato, J. A. L. Perini, L. D. de M. Torquato, M. V. B. Zanoni, *J. CO2 Util.* **2022**, *55*, 101810.
- [67] J. F. de Brito, M. V. B. Zanoni, *Chem. Eng. J.* **2017**, *318*, 264.
- [68] J. F. Brito, A. R. Araújo, K. Rajeshwar, M. V. B. Zanoni, *Chem. Eng. J.* **2015**, *264*, 302.
- [69] J. F. de Brito, P. G. Corradini, A. B. Silva, L. H. Mascaro, *ChemElectroChem* **2021**, *8*(22), 4305.
- [70] N. Zhang, A. Jalil, D. Wu, S. Chen, Y. Liu, C. Gao, W. Ye, Z. Qi, H. Ju, C. Wang, X. Wu, L. Song, J. Zhu, Y. Xiong, *J. Am. Chem. Soc.* **2018**, *140*(30), 9434.
- [71] C. Guo, J. Ran, A. Vasileff, S. Z. Qiao, *Energy Environ. Sci.* **2018**, *11*(1), 45.
- [72] M. B. Costa, F. W. de S. Lucas, L. H. Mascaro, *ChemElectroChem* **2017**, *4*(10), 2507.
- [73] A. D. Collord, H. W. Hillhouse, *Chem. Mater.* **2016**, *28*(7), 2067.
- [74] A. L. Woodley, C. F. Drury, W. D. Reynolds, W. Calder, X. M. Yang, T. O. Oloya, *Can. J. Soil Sci.* **2018**, *98*(2), 193.

---

Manuscript received: July 18, 2024

Revised manuscript received: September 30, 2024

Accepted manuscript online: October 21, 2024

Version of record online: November 24, 2024